AGU PUBLICATIONS

Journal of Advances in Modeling Earth Systems

RESEARCH ARTICLE
10.1002/2014MS000390

The behavior of trade-wind cloudiness in observations and models: The major cloud components and their variability

Louise Nuijens[1], Brian Medeiros[2], Irina Sandu[3], and Maike Ahlgrimm[3]

[1]Atmosphere in the Earth System Department, Max Planck Institute for Meteorology, Hamburg, Germany, [2]Climate and Global Dynamics Division, National Center for Atmospheric Research, Boulder, Colorado, USA, [3]Physical Aspects Section, European Centre for Medium-Range Weather Forecasts, Reading, UK

Key Points:
- Models fail to couple cloud near cumulus tops with cloud near cumulus bases
- Models vary the wrong component of trade-wind cloudiness
- Models do not capture the processes that underlie cloud changes

Correspondence to:
L. Nuijens,
louise.nuijens@mpimet.mpg.de

Citation:
Nuijens, L., B. Medeiros, I. Sandu, and M. Ahlgrimm (2015), The behavior of trade-wind cloudiness in observations and models: The major cloud components and their variability, *J. Adv. Model. Earth Syst.*, *7*, 600–616, doi:10.1002/2014MS000390.

Received 24 SEP 2014
Accepted 24 MAR 2015
Accepted article online 27 MAR 2015
Published online 23 APR 2015

Abstract Guided by ground-based radar and lidar profiling at the Barbados Cloud Observatory (BCO), this study evaluates trade-wind cloudiness in ECMWF's Integrated Forecast System (IFS) and nine CMIP5 models using their single-timestep output at selected grid points. The observed profile of cloudiness is relatively evenly distributed between two important height levels: the lifting condensation level (LCL) and the tops of the deepest cumuli near the trade-wind inversion (2–3 km). Cloudiness at the LCL dominates the total cloud cover, but is relatively invariant. Variance in cloudiness instead peaks at the inversion. The IFS reproduces the depth of the cloud field and its variability, but underestimates cloudiness at the LCL and the inversion. A few CMIP5 models produce a single stratocumulus-like layer near the LCL, but more than half of the CMIP5 models reproduce the observed cloud layer depth in long-term mean profiles. At single-time steps, however, half of the models do not produce cloudiness near cloud tops along with the (almost ever-present) cloudiness near the LCL. In seven models, cloudiness is zero at both levels 10 to 65% of the time, compared to 3% in the observations. Models therefore tend to overestimate variance in cloudiness near the LCL. This variance is associated with longer time scales than in observations, which suggests that modeled cloudiness is too sensitive to large-scale processes. To conclude, many models do not appear to capture the processes that underlie changes in cloudiness, which is relevant for cloud feedbacks and climate prediction.

1. Introduction

Shallow cumulus convection, which covers substantial areas over the subtropical oceans, is a major source of uncertainty in the prediction of climate sensitivity [*Bony and Dufresne*, 2005; *Medeiros and Stevens*, 2011; *Vial et al*., 2013]. Climate models predict different responses of cumulus clouds to a warming climate and therefore different changes in cloud radiative effects, predominantly in the shortwave component. The uncertainties do not only exist in a future climate, the shortwave cloud radiative effect (SWCRE) is also biased in the current and past climate. The albedo of clouds and therefore the SWCRE is on average overestimated compared to observations, especially in regions of moderately subsiding motion where shallow trade-wind cumuli prevail. The models tend to make the clouds in these regions too bright, to compensate for the fact that there are too few of them [*Nam et al*., 2012].

Recent work hints that the modeled spread in future cloud responses is caused by the same physical processes that cause biases in present-day cloudiness. These processes start to explain why some models are low-sensitivity models and others are high-sensitivity models. *Sherwood et al*. [2014] show that different cloud responses may be partly attributed to a poor representation of the mixing of heat and moisture in the lower troposphere. Models that efficiently distribute moisture in the vertical in the present-day climate are more prone to dry out the lower troposphere and reduce cloudiness as climate warms, which results in a positive cloud feedback and a higher climate sensitivity. Brient et al. (F. Brient, T. Schneider, Z. Tan, and S. Bony, Shallowness of tropical low clouds as a predictor of climate models response to warming, submitted to *Climate Dynamics*, 2015). furthermore show that models with a high climate sensitivity have a large peak in cloud fraction near cloud base, resembling more a stratocumulus layer than a cumulus layer. Models with a more realistic cloud fraction profile, whereby cloudiness is more evenly distributed across a deeper boundary layer, are found to be less sensitive to warming.

The vertical distribution of low-level clouds is thus emerging as a key feature that needs to be understood because it reflects how moisture and clouds are distributed by the model. This theme serves as the basis for

this manuscript, in which we describe whether models reproduce the major components of the vertical structure of trade-wind clouds and their variability. We do so in the framework of recent ground-based observations at the Island of Barbados, a location downstream of typical trade-wind trajectories across the North-Atlantic. At this location, cloud cover can be decomposed into contributions from two main components of the cloud field, which appear controlled by different mechanisms. The first important component includes clouds that are present at heights near the lifting condensation level (LCL), roughly below 1 km. The second component includes clouds that are present at heights further aloft, above 1 km. Clouds near the LCL include both positively buoyant cloud cores as well as passive (detrained) cloud. On average, it contributes two-thirds to the total projected cloud cover [*Nuijens et al*., 2014]. Cloud further aloft contributes another third to total cloud cover, but only when there is no corresponding cloud (base) at levels below. Large contributions from cloudiness aloft to cloud cover occur when clouds are deeper and do not efficiently overlap with cloud below it, as well as when stratiform layers form near the detrainment level of cumulus tops, near the inversion.

Cloudiness aloft has considerable variance on time scales of a day to a week, whereas cloudiness near the LCL is relatively invariant on those time scales. This appears true across a range of large-scale conditions, including the change from the dry Winter to the wet Summer season. An explanation may be sought in the processes that control these two components [*Nuijens et al*., 2014]. Cloudiness near the LCL is constrained by cumulus convection and the turbulent processes in the mixed-layer, which quickly adjust to perturbations in the large-scale flow [*Neggers et al*., 2006; *Bellon and Stevens*, 2013]. Cloudiness aloft in turn may depend on whether gradients, shear, or strong subsidence are present aloft. Those processes may vary on time scales longer than a day.

In this study, we explore how large-scale models represent these components of cloudiness and their variability. We do so by not only looking at long-term means, but also at shorter timescales. The latter may reveal how sensitive modeled clouds are to changes in the environment. In particular, we ask: do models have a cloud structure that is similar to that observed, including the presence of cloudiness near the LCL and cloudiness near cloud tops? Furthermore, do models reproduce the relative invariance of cloudiness near the LCL on longer time scales?

Our analysis makes use of single-timestep output of models, which is available at selected locations as part of a Climate Model Intercomparison Project phase 5 (CMIP5) initiative. Nine CMIP5 models provide this output. Additionally, high-resolution short-range forecasts obtained with the Integrated Forecast System (IFS) from the European Centre for Medium-Range Weather Forecasts (ECMWF) are used for an area equivalent to the size of a climate model grid box. The location chosen is nearby or upstream of the island of Barbados.

The manuscript is structured as follows: a detailed description of the data sources and our methods is given in section 2. This is followed by a description of the mean structure of cloud and its environment in the observations (section 3.1) and the models (section 3.2). Section 4 presents an analysis of the prevailing variability in cloudiness in all three data sources, and the main findings are summarized in section 5.

2. Data and Methods

The three data sources that we use are ground-based radar, lidar, and ceilometer data from the BCO, forecasts obtained with the Integrated Forecast System (IFS) from the European Centre for Medium-Range Weather Forecasts (ECMWF) model and single-timestep output from a subset of CMIP5 models. These data differ in many respects, from their basic definition of cloud to their resolution and time period covered. In the following sections, each data source is described in detail (section 2.1–2.3) and the methods and terminology that we apply to compare these inherently different data sets is explained (section 2.4).

2.1. Ground-Based Remote Sensing

The BCO is located on an eastward promontory of the island of Barbados (13.15°N, 59.4°W) and has a suite of instrumentation similar to the Department of Energy (DOE) ARM sites. The period April 2010 to April 2012 is used for deriving cloud statistics from different instruments, of which a detailed description is provided in *Nuijens et al*. [2014]. A shorter description of the products that are used in this analysis follows here.

Cloud cover (CC) is measured with a ceilometer, and defined as the fraction of time with a cloud base height overhead. By separating cloud bases that are detected below or above 1 km, we separate the effective contribution of cloud at heights near the lifting condensation level to cloud cover (hereafter referred to as CC_{LCL}) from cloud at heights further aloft (CC_{ALOFT}). The time series of cloud cover is almost continuous during the above 2 year period, and therefore our main data source for deriving statistics.

Cloud fraction (CF) profiles are derived from the Ka band (36 GHz) Doppler radar (KATRIN), which operated from January 2011to mid-May 2011 and in October 2011 in an alternating vertical pointing and scanning mode and from January 2012 to March 2012 in vertically pointing mode only. Only data from the vertical pointing mode is used, which includes a profile every 10 s with a resolution of 30 m from 300 m up to 15 km. When performing spectral analysis, the data period is restricted to the period January 2012 to March 2012, which is the only period during which the radar was in continuous vertical pointing mode without downtimes. Those radar returns with an equivalent radar reflectivity Z_e greater than -40 dBZ are defined as true hydrometeor returns. This is a rather conservative threshold, which implies that the hydrometeor fraction is underestimated. For a discussion of the sensitivity of cloud amount to the thresholds applied we refer the reader to *Nuijens et al*. [2014]. To exclude rain from the CF profile, periods during which rain rates of more than 0.05 mm h^{-1} are present in at least five range gates of the vertically operating 24 GHz FMCW radar (the micro rain radar, MRR) are excluded. Additionally, all returns below the lowest detected cloud base height from the ceilometer, which indicate drizzle, are masked.

Humidity and temperature profiles are measured with a multichannel Raman lidar, from 1 April 2011 to 1 April 2012. By measuring backscattered energy at the shifted Raman frequency, in the UV spectral range at 355 nm, the concentration of water vapor is derived. Furthermore, by making using of the pure rotational Raman spectra (PRRS) technique, air temperature is derived [*Serikov and Bobrovnikov*, 2010]. The profiles of humidity and temperature are only available during nighttime when there is no interference of background solar light, between 0 and 8 UTC (20:00–04:00 h local time). In addition, the lidar hatch closes during periods of rain, identified from the MRR when it measures rain rates >0.05 mm h^{-1} at any height below 3 km. To achieve enough accuracy, the raw data are averaged into 2 min profiles for water vapor and 1 hourly profiles for temperature, available at a 60 m resolution up to 15 km.

2.2. ECMWF IFS

We use both short-range forecasts and long climate-like integrations produced with the ECMWF IFS. For the short-range forecasts, we use lead times of 12–33 h of the operational high-resolution 10 day forecasts produced daily by ECMWF between 1 April 2010 and 1 April 2012. These forecasts are produced at a T1279 horizontal resolution, at which a grid box comprises roughly 16 by 16 km at the equator. Because we use the forecasts initialized at 12 UTC from the ECMWF analyses, these lead times correspond to 0–21 UTC the next day. For this interval, model output was extracted every 3 h, for 5×3 grid boxes situated in an area of about 75×45 km^2 upstream of Barbados (13.14–13.42°N, 59.06–58.5°W). The results of the short-range forecasts discussed hereafter, denoted as ECMWF in the figures and tables, represent an average over these 15 grid boxes.

The long integrations are 1 year long forecasts initialized on 1 August, performed at a horizontal resolution of T255, at which a grid box comprises roughly 75 by 75 km at the equator. These are climate-like integrations that do not start every day from a state that is corrected by data assimilation procedures, such as in the short-range forecasts. The output is therefore comparable to the CMIP5 model output that we use. Four long integrations were performed with an IFS version that was operational between June 2013 and November 2013 (IFS Cycle 38r2), for the years 2009–2012, which cover the period of the BCO observations. Instantaneous (30 min) output is extracted from all these runs for a single grid point near Barbados (centered at 13.68°N, 59.06°W). In the results discussed hereafter, we denoted these as ECMWF-LI in the figures and tables. Both the short-range forecasts and the long-integrations were performed using 91 vertical levels. In this study, we only use the output for the lowest 31 levels, reaching from 10 to 7600 m with an interval of 20 m at level 1 and 500 m at level 31.

2.3. cfSites Output From CMIP5 Models

Single-timestep output of a subset of climate models for a single grid point near Barbados is used, which is available through the cfSites initiative. This initiative has collected single-timestep model output for about

Table 1. List of Models used in the Analysis, Including the Number of Model Levels up to 600 hPa (L_{600hPa}), and between 950–900 hPa (L_{900hPa}), and References to their Cloud and Convection Schemes[a]

No.	Abbreviation	Model	Modeling Center	$L_{600hPa/900hPa}$	Cloud/Convection Scheme
1	ECWMF	IFS short integration	European Centre for Medium-Range Weather Forecasts	24/3	*Tiedtke* [1993]/*Tiedtke* [1989]
2	ECWMF-LI	IFS Long integration	" "	" "	" "
3	MPI-M	MPI-ESM-LR	Max-Planck Institute for Meteorology	11/2	*Tiedtke* [1989]/*Sundqvist et al.* [1989]
4	BCC	BCC-CSM1.1	Beijing Climate Center	7/1	*Wu et al.* [2010]/*Slingo* [1987]
5	CCCma	CanESM2	Canadian Centre for Climate Modelling and Analysis	14/2	*von Salzen et al.* [2005]/*McFarlane et al.* [2005]
6	IPSL	IPSL-CM5A-LR	Institut Pierre-Simon Laplace	11/1	*Bony and Emanuel* [2001]/*Emanuel* [1993]
7	CNRM	CNRM-CM5	Centre National de Recherches Meteorologiques	11/2	*Gregory and Rowntree* [1990]/*Ricard and Royer* [1993]
8	MOHC	HadGEM2-A	Met Office Hadley Centre	14/2	*Gregory and Rowntree* [1990]/*Lock* [2009]
9	MRI	MRI-CGSM3	Meteorological Research Institute	12/1	*Yukimoto et al.* [2012]/*Tiedtke* [1993]
10	NCAR-C4	CAM4	National Center of Atmospheric Research	7/3	*Rasch and Kristjansson* [1998]/*Zhang and McFarlane* [1995]
11	NCAR-C5	CAM5	National Center of Atmospheric Research	11/5	*Gettelman et al.* [2010]/*Zhang and McFarlane* [1995]

[a]All models use the BOMEX location, except the ECMWF and ECMWF-LI and MPI-M, which use a grid point just upstream of Barbados. All models have output every 30 min, except for the ECMWF, which is extracted at 3 hourly intervals. For the BCC and NCAR-C4 model, only every second output step is used in the analysis, see section 2.3.

120 grid point locations around the globe as part of the Cloud Feedback Model Intercomparison Project (CFMIP). The standard grid point locations include important transects and locations where past field campaigns took place and on which modeling studies have focused, or where observational super sites are located. The output from control experiments is used, which are Atmospheric Model Intercomparison Project (AMIP) runs from 1976 to 2006, constrained by observed sea surface temperature and sea ice. The CMIP5 models and their acronyms are listed in Table 1. With the MPI-ESM, model output has been created for a grid point near the BCO (13.2°N 59.4°W), whereas the nearest location for other models is the BOMEX location (15°N 56.5°W). For all models, these grid points correspond to an area of about 100 × 100 km^2. The statistics for the BCO location and the BOMEX location appear qualitatively similar for the MPI-ESM, and we believe the BOMEX location largely suffices in exploring cloud behavior, except that it tends to experience fewer periods with mean rising motion.

For MPI-M, we thus do not use the data in the CMIP5 archive, but have rerun the model with the newer ECHAM version 6.2, wherein errors in the way that the statistics are accumulated have been fixed. For most models single-timestep output means 30 min output, except for the BCC model, which comes at a 20 min resolution. However, for the BCC model, it appears that two out of three time steps have zero cloud fractions everywhere, which seems an issue with the way the output has been produced. Hence, we only use every third time step from their data. The same is true for the NCAR-C4 model, which has zero cloud fractions every other time step. Although 30 years of data is available, 5 years (2001–2006) largely suffices for most of our analysis.

2.4. Cloud Fraction and Cloud Cover in the Observations and the Models

Cloudiness in models and in observations are inherently different. An often used technique to overcome these differences and compare models with observations is to use forward operators or cloud simulators implemented in models. These simulate how cloud predicted by the model would be measured by a given instrument. However, our analysis focuses on qualitative rather than quantitative behavior of cloudiness. For instance, we study the shape of the cloud fraction profile or the variability of cloud fraction in time. To identify differences in such qualitative aspects between models and observations, it is not necessary to apply a forward operating technique. For a similar reason, we also do not interpolate the observations onto a coarser vertical grid that is representative of the model's grid.

We do account for the difference in temporal or horizontal resolution: the observations have a footprint of just a few tens of meters, whereas a single model grid point is equivalent to an area of about 100 km^2. The BCO time series is first averaged to a period that represents the time needed for an air mass to travel across a 100 km distance. Wind speeds are observed to be about 7 ms^{-1} on average, which equals four hour of BCO measurements. In all figures and analysis where time scales are mentioned, the averaging of the BCO data is implicit, unless we explicitly state otherwise.

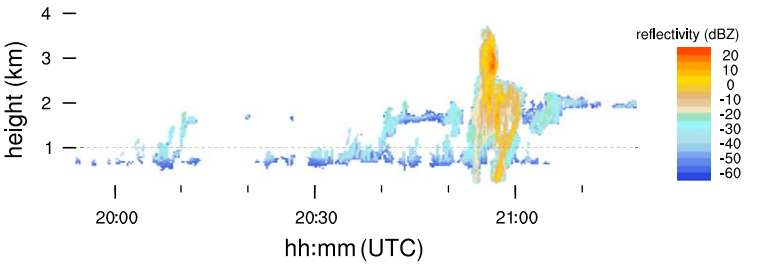

Figure 1. An example of the low-level cloud field as observed by the cloud radar at the BCO between 20:00 and 21:30 UTC on 7 March 2012. The radar reflectivity is shown, which effectively measures the sixth moment of the drop size distribution, and is thus especially sensitive to large drops.

CF refers to the amount of cloud that is present at a given height or pressure level, whereas CC is the total amount of cloud projected onto the surface. The observational record of CF is intermittent due to frequent downtimes of the cloud radar (section 2.1). Therefore, we often use the more continuous time series of CC instead. By distinguishing between CC that arises from cloud bases detected below 1 km (CC_{LCL}) or above 1 km (CC_{ALOFT}), we qualitatively capture the two dominant components of the cloud fraction profile that are observed in this region [*Nuijens et al.*, 2014]. CC always refers to cloud that is present at heights below 5 km ($\approx$ 550 hPa).

When rainfall is strong enough, the ceilometer cannot detect a cloud base height. This is true for 60% of the rain events. Because the total rain cover is 0.07 [*Nuijens et al.*, 2014], this means that for 4.2% of the observed profiles we cannot meaningfully separate the two components of CC_{LCL} and $CC_{ALOFT.}$ For these 4.2%, we also cannot assess whether hydrometeors measured by the radar represent rain that falls through a detectable cloud base or rain that falls through the cloud layer out of slanted clouds. In our derivation of CC and CF, we exclude these 4.2% of data. This means that we underestimate total cloudiness in the observations by excluding heavily raining cloud, a bias we are willing to accept given our focus on qualitative behavior. Because these cases comprise only 4.2% of the record, they also do not substantially bias our results. Namely, if we include rain hydrometeors into the profile of CF [see *Nuijens et al.*, 2014, Figure 4a], none of our conclusions on the shape of the cloud profile and its variability with time and across seasons change (not shown). We nevertheless exclude the rain hydrometeors where we can, because this more clearly exposes the location of cloud base.

The model output does not provide CC for clouds at heights below 5 km only. For the CMIP5 models, we therefore use CF at selected levels to assess cloudiness, such as near the cloud base or near the observed inversion height (825 hPa). Because many models just have one or two vertical levels between 950 and 900 hPa, corresponding to the mean LCL and 1 km (Table 1), their CC_{LCL} is basically equal to or very close to CF at those levels. Hence, in comparing qualitative behavior of cloudiness, we freely compare CC_{LCL} or CC_{ALOFT} for the observations with the CF at selected levels for the models. Only for the ECMWF, we use an offline version of IFS's cloud overlap routines to derive the CC, CC_{LCL}, and $CC_{ALOFT,}$ and compare this to the observations.

3. Structure of Cloud and the Environment

3.1. Observations

The dominant cloud type in the trades is trade-wind cumulus. Trade-wind cumuli typically occur in the form of shallow cumulus humilis with cloud tops near 1–1.5 km, as well as in the form of deeper cumuli reaching up to 2 or 3 km, which are often accompanied by rain and sometimes accompanied by a layer of stratiform outflow near their tops [*Nuijens et al.*, 2014]. A radar quicklook in Figure 1 nicely illustrates all these cloud types passing the BCO within a period of about 1.5 h, whereby the colored contours refer to the equivalent radar reflectivity Z_e. From cloud base to cloud top Z_e increases with the increase in liquid water content and the growth of cloud droplets. When rain drops have formed, large values of Z_e (>-20 db$Z$) are observed.

The signature of these different cloud types is also apparent in the distribution of 4 hourly cloud fraction (CF) as a function of height (Figure 2a). The mean and median profiles are shown as solid and dotted lines, respectively, whereby their difference is a measure of the skewness of the distribution. The shaded area

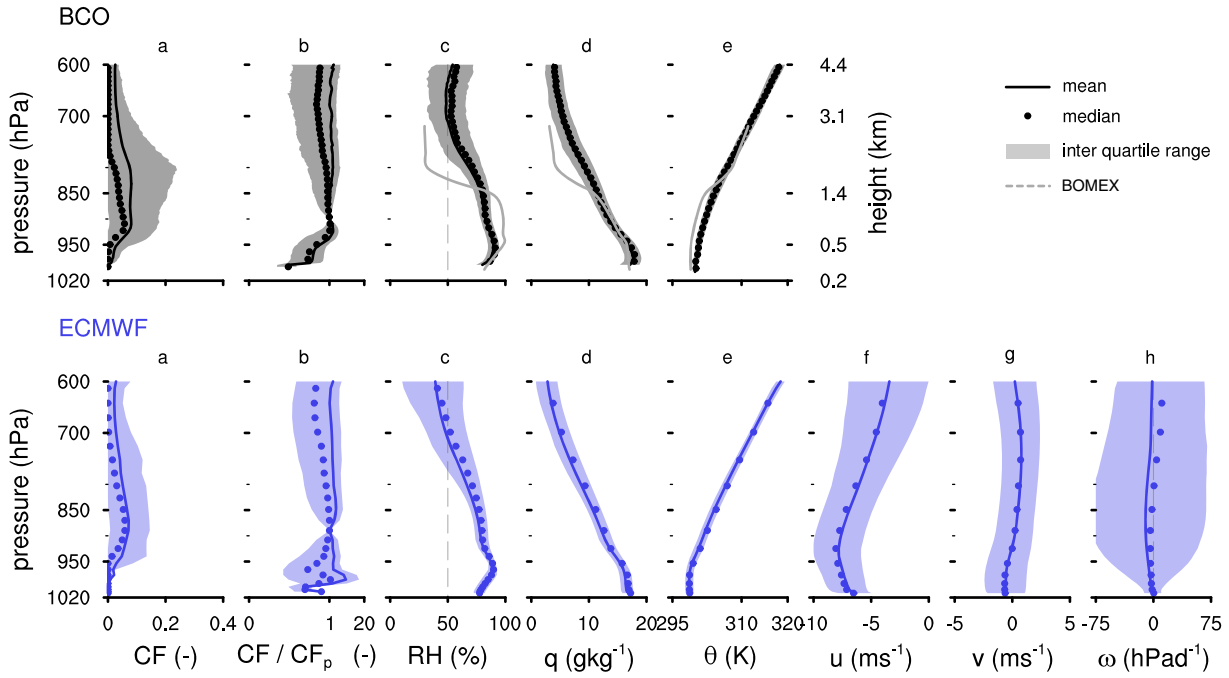

Figure 2. The vertical structure of cloud and its (thermo)dynamic environment upstream of Barbados, from ground-based observations at the Barbados Cloud Observatory (BCO) at 13°N, 59°W and ECMWF short-range forecasts over a region ≈ 75 km × 45 km east and north of the BCO for the period 1 April 2010 to 1 April 2012. Illustrated are the mean profile (solid line) and median profile (circles) as well as the interquartile range (shaded polygons) for 4 hourly values of (a) cloud fraction (CF), (b) the ratio of CF over CF_p where p refers to p_{CFmax} (see text and Table 2), (c) the relative humidity (RH), (d) the specific humidity (q), (e) the potential temperature θ, (f) the zonal wind component u, (g) the meridional wind component v, and (h) the vertical velocity ω. Note that CF/CF_p is shown on a log-scale. The gray dotted lines indicate the profiles of the Large-Eddy Simulation case based on the mean BOMEX sounding.

refers to the interquartile range of CF. Both the mean and the median CF peak at 925 hPa, where the LCL is typically located. The median profile then slowly decreases with height, which is a typical profile for the shallower trade-wind cumuli during the first hour depicted in Figure 1. The mean profile instead is relatively constant with height. This is because deeper clouds tend to be wider clouds and accompanied by stratiform outflow layers near their tops, such as the cloud just before 21:00 UTC in Figure 1 [see *Nuijens et al.*, 2014, also Figure 5]. The interquartile range shows that some 4 h periods even have a CF near 800 hPa of 0.3.

Variations in the shape of the CF profile from one period to the next may be measured by the ratio of CF to CF near cloud base ($CF_{p)}$ in each 4 hourly averaged profile. We take cloud base as the level where the mean CF profile maximizes ($p_{CFmax)}$, which must be at a pressure > 850 hPa to target levels near the LCL. For the observations, p_{CFmax} is close to 920 hPa (Table 2). If in a particular profile the ratio of CF to CF_p equals 1 at

Table 2. The Pressure Level (p > 850 hPa) at Which the Mean CF Profile Maximizes, the Percentage of Profiles at Which CF Equals Zero at Both 925 and 825 hPa, the Total Variance in $CF_{p,}$ the Total Variance in CF_{825} and Lastly, the Ratio of the Variance in CF_{825} to the Variance in CF_p[a]

No.	Abbreviation	p_{CFmax} (hPa)	$CF_{925/825} = 0$(%)	$\sigma^2[CF_{p]}$ (-)	$\sigma^2[CF_{825]}$ (-)	σ^2ratio (-)
0	BCO	920	3	0.009	0.016	1.8
1	ECMWF	870	6	0.010	0.007	0.7
2	ECMWF-LI	870	6	0.008	0.008	1.0
3	MPI-M	941	44	0.109	0.000	0.0
4	BCC	945	4	0.018	0.024	1.3
5	CCCma	911	16	0.058	0.002	0.03
6	IPSL	953	64	0.017	0.003	0.2
7	CNRM	904	65	0.074	0.040	0.5
8	MOHC	901	11	0.016	0.013	0.8
9	MRI	896	26	0.010	0.021	2.1
10	NCAR-C4	867	51	0.019	0.020	1.0
11	NCAR-C5	913	1	0.010	0.005	0.5

[a]We note that the percentage of profiles whereby CF equals zero at all levels below 800hPa is zero in all models and observations, e.g., there is usually cloud present at least at one level.

all height levels, the CF profile for that period is constant with height. Instead, if the ratio increases with height the profile is top-heavy and if the ratio decreases with height the profile is bottom-heavy. The mean, median, and interquartile range of the ratios of CF to CF_p for all profiles is shown in Figure 2b). At most levels, the mean and median do not deviate much from 1, which implies that even in individual profiles cloudiness is distributed fairly equally across the depth of the cloud layer.

Qualitatively, these results do not change if we use a different threshold of Z_e to define cloud (section 2.1) or if we include rain hydrometeors (section 2.4). Choosing a smaller Z_e threshold will increase CF at those levels where thin clouds are present, which is near the LCL and near the inversion. Including rain hydrometeors will also increase CF by about 0.04 at most levels [see *Nuijens et al*., 2014, Figure 4a]. However, these increases do not substantially change the shape of the cloud profile and its variability with time (not shown). Furthermore, such changes are still an order of magnitude smaller than the spread in CF among models (section 3.3).

The humidity and temperature profiles exhibit some key features of the trades that have been described in past studies. One notable feature is the decrease in specific humidity at the top of the mixed-layer near 920 hPa, often called the transition layer [*Malkus*, 1958]. This layer is close to the location of the LCL. The deepest cloud tops are instead typically located near the trade-inversion, a signature of which is seen near 800 hPa in both the humidity and temperature profiles. Compared to the Barbados Oceanographic and Meteorological Experiment (BOMEX) case study [*Siebesma et al*., 2003], the trade-wind inversion at the BCO is less pronounced and the cloud layer is deeper and more humid (Figures 2c–2e). A couple of reasons may explain these differences. The cloud layer may be deeper due to the location of Barbados, which is downstream of the 500×500 km^2 area in which BOMEX was conducted. A comparison of low-level cloud cover from MODIS, in an area upstream of Barbados, with that measured at Barbados also suggests that cloud top heights and cloudiness increase toward the island [*Brueck et al*., 2015]. What may also play a role is the large-scale environment that Barbados experienced during 2010–2012, which deviates from the climatology. The mean vertical motion was on average -20 hPad^{-1} (see also the ECMWF IFS profiles in Figures 2h–2j). In addition, sea surface temperatures were higher and winds were weaker compared to previous years. Similar (deviating) conditions were present during 2005 when the Rain in Cumulus over the Ocean field campaign (RICO) was conducted [*Rauber et al*., 2007]. Indeed, the clouds produced with LES of the RICO case study also reach cloud top heights near 3 km and are accompanied by outflow layers near cloud tops [*VanZanten et al*., 2011]. Therefore, both RICO and the BCO appear representative of a more vigorous (downstream) trade-wind regime, whereas the BOMEX case studied by *Siebesma et al*. [2003] represents a shallower cloud field.

Despite its downstream location, Barbados does experience periods in which mostly the shallower cumulus humilis cloud type prevails. Results presented in section 4.2 show that there is a notable seasonality in the cloud profile. The summer profile reflects a field with predominantly cumulus humili and is similar to the *median* profile in Figure 2a. The winter profile instead reflects the deeper cumuli and is similar to the *mean* profile in Figure 2a. Therefore, the different cloud fields observed during different measurement periods may to a large extent be explained by seasonality and prevailing large-scale conditions at the time. All of those cloud fields can be considered typical for the trades. Indeed, other days during BOMEX not studied by *Siebesma et al*. [2003] had much deeper convection [*Nitta and Esbensen*, 1974].

The different cloud fields contribute differently to the projected cloud cover (CC), whose distribution is shown in black lines in the left plot of Figure 3. CC is dominated by contributions from clouds who have their bases within a close distance to the LCL, CC_{LCL} (second plot). These can be either from shallow clouds or deeper clouds. The other contribution to CC is denoted as cloudiness aloft, $CC_{ALOFT,}$ which is on average smaller and more frequently close to zero (third panel). CC_{ALOFT} becomes larger positive as clouds get deeper, simply because clouds tend to be irregularly shaped and often tilted by wind shear, so that cloud at different levels does not efficiently overlap. Overlap ratios are estimated to be 0.2–0.3 [*Nuijens et al*., 2014], consistent with previous studies that noted the inefficient overlap of cumuli. CC_{ALOFT} also increases when stratiform layers form near tops of clouds just underneath the inversion or when clouds lose their roots in the subcloud layer and are left as decaying patches at heights above 1 km. By analyzing the duration and depth of each cloud entity separately, we find that on average per day, short-lasting patches of cloud contribute 20% to cloudy periods. Here, short lasting is less than 12 consecutive radar profiles (2 min). Of these clouds, the average contribution of cloudiness aloft to the cloud length is 20% [*Nuijens et al*., 2014].

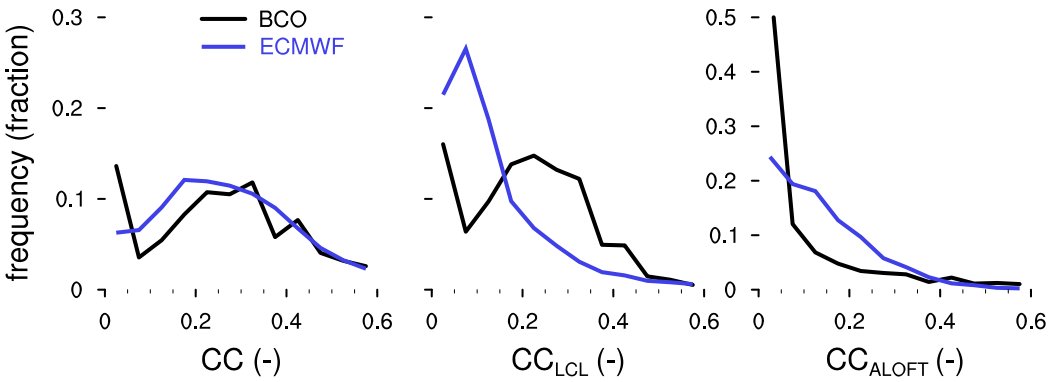

Figure 3. Frequency distribution of CC, CC_{LCL}, and CC_{ALOFT} derived from 4 hourly ceilometer data at the BCO (in black) and from each ECWMF IFS forecast (in blue). For the ECMWF, an offline calculation of cloud overlap is applied to calculate the cloud covers, see section 2.2. Tickmarks on the *x* axis correspond to the frequency bins used.

Combining these numbers, we may therefore estimate that for this particular cloud type the contribution of cloudiness aloft to CC is about 4%. Repeating this exercise for the longer-lasting cloud entities that reach at least 1.5 km, we find that for clouds without a stratiform component cloudiness aloft contributes about 8% to CC. Finally, for clouds that do have a stratiform component cloudiness aloft contributes 13% to CC. Therefore, especially when clouds get deeper and when stratiform outflow forms, the effective contribution of CC_{ALOFT} to CC becomes larger.

3.2. Numerical Weather Prediction Forecasts

The cloud profile produced in the short-range forecasts with the ECMWF IFS is largely determined by the model's convection parameterization [*Tiedtke*, 1989; *Bechtold et al*., 2008] and cloud scheme [*Tiedtke*, 1993]. Compared to other models, the IFS' entrainment and detrainment processes perform well [*de Rooy et al*., 2013]. The median profile of cloud in the IFS is close to the observed median profile. The model distributes clouds fairly evenly across the cloud layer, leading to frequent ratios of CF to CF_p that are close to 1 (Figures 2a and 2b). Cloud fractions are somewhat too small, especially given that the observed profile is an underestimation of real CF, which is a feature of the IFS that has been reported before [*Ahlgrimm and Köhler*, 2010]. The model also occasionally forms what might be fog layers very close to the surface at 980 hPa, which leads to a large skewness in the ratio of CF to CF_p at that level (Figure 2b).

Compared to the observations the IFS misses a pronounced peak in CF near cloud base and the CF distribution is much less skewed near 800 hPa. This suggests that the model does not reproduce the ensemble of clouds that is observed, which includes both the shallower cumulus humuli along with the deeper cumuli that can have outflow layers. The total CC produced by the IFS is comparable to the observations (blue lines in Figure 3), but CC_{LCL} is underestimated and CC_{ALOFT} is overestimated. Part of the underestimation of CC_{LCL} might be caused by the modeled clouds falling into the CC_{ALOFT} category rather than into the CC_{LCL} category, because CF in the IFS on average peaks at a level just above 1 km.

Explanations for the absence of peaks in CF near the LCL and near the inversion may be sought in the lack of vertical resolution or deficiencies in the parameterized physics, such as a too efficient mixing of moisture across the inversion, or biases in detrainment. The mixing of moisture and the detrainment appear key to the problem, because a further increase in vertical resolution from 91 to 137 levels, which adds an additional 16 levels at heights below 500 hPa, does not lead to any major improvement in the cloud profile (not shown). Data assimilation procedures may also play a role. As will be shown in the next section, the ECMWF-LI simulation, without data assimilation, exhibits a larger cloud fraction near 850 hPa. This suggests that through data assimilation procedures the structure of the boundary layer may be distorted. For instance, the trade-wind inversion is weakened, which in turn may lead to fewer stratiform layers.

Another deficiency of the model (and for most models) is that liquid water in the cloud updraft, the cloud core, is not fed into the cloud scheme, and thereby does not contribute to the cloud fraction and cloud cover. CF at cloud base is about 10%. This includes the active cloud core with a CF of 1–8% and the passive detrained cloud with a CF of 0–5% (not shown). Models thus principally underestimate trade-wind

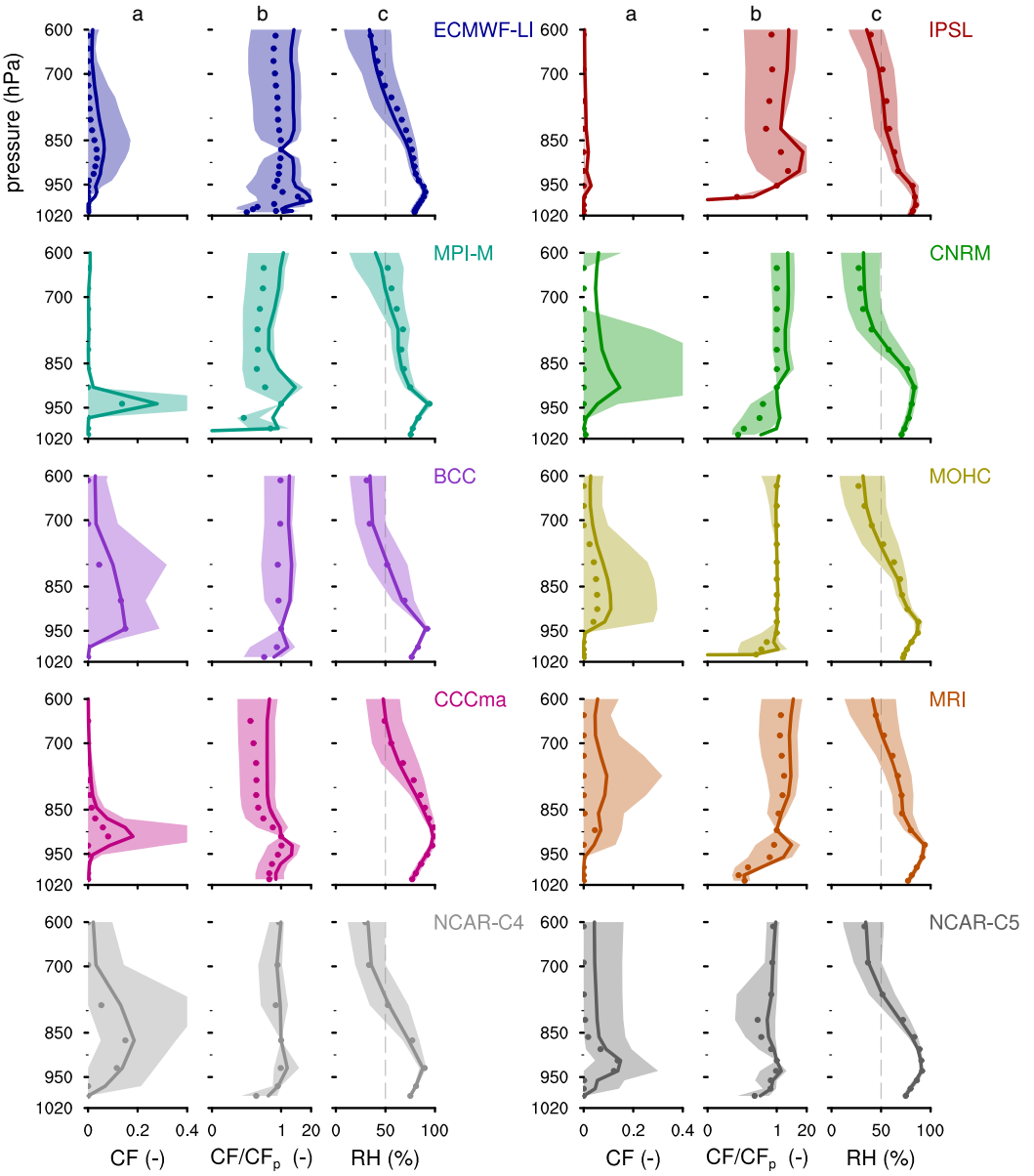

Figure 4. Similar to Figure 2: the mean profile (solid line), median profile (circles), and the interquartile range (shaded polygons) of the distributions of the following parameters: (a) cloud fraction (CF), (b) the ratio of CF over CF_p, where CF_p is CF at p_{CFmax} (Table 2), and (c) the relative humidity (RH). The distributions are derived from single-timestep (30 min) output of climate models at a single grid point (the Barbados or BOMEX location), see Table 1.

cloudiness. Although many models likely have much larger issues to solve first, for the IFS this could possibly bring the predicted CF profile markedly closer to the observations.

Day-to-day variability in the IFS temperature and humidity profiles match that of the observations (not shown), but the IFS is on average 1–2 g kg^{-1} drier near 900 hPa, whereas the free troposphere between 750 and 700 hPa is 1–2 g kg^{-1} more humid. The forecasts are also about 1 K colder. This indicates that the model's vertical mixing might be too efficient, which is in fact a known feature of the model. The slightly too active mixing is tolerated, because it leads to an improved model performance in the tropics by means of other metrics such as deep convective activity, precipitation, and winds. Overall, the agreement is good enough to make use of the modeled zonal and meridional winds to infer relationships between the large-scale flow and cloud types. However, this may not be true for the vertical velocity, which is the parameter that is least constrained by observations in the 12 UTC analysis.

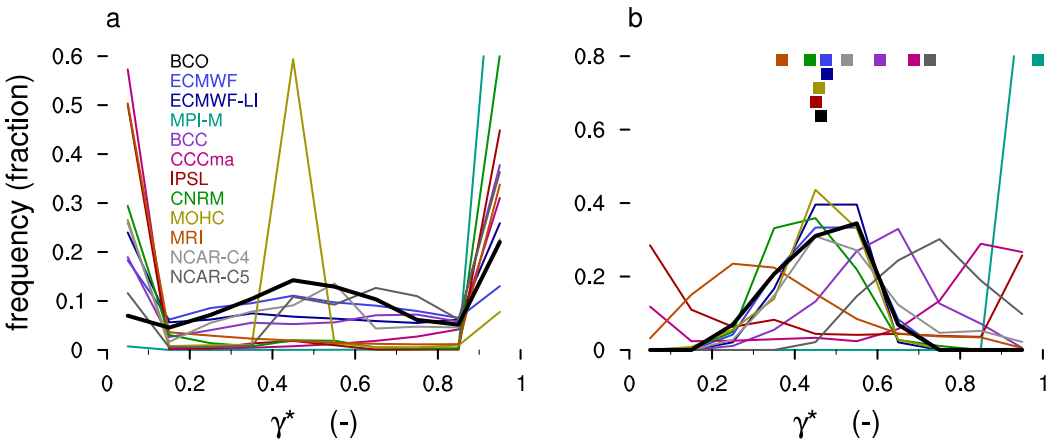

Figure 5. The frequency distribution of γ^* using single-timestep CF profiles (a) and monthly mean CF profiles (b), where the tickmarks on the *x* axis correspond to the frequency bins used. A modified γ^*, after Brient et al. (submitted manuscript, 2015), is defined as $CF_{925}/(CF_{925}+CF_{825})$. From $\gamma^* = 0$ to $\gamma^* = 1$, the cloud fraction profile moves from being top-heavy to bottom-heavy. The frequency of finding $\gamma^* = 0$ because CF at both 925 and 825 hPa = 0 is shown in Table 1. At the top of Figure 5b, the mean γ^* of the monthly mean distribution is shown as a square marker.

3.3. Climate Models

The climate-like long integration of the IFS (ECMWF-LI) performs similar to the short-range forecasts, perhaps even somewhat better. Its CF profile in Figure 4a reveals a more skewed distribution near 850 hPa. The long integration thus more frequently supports clouds that deepen up to that level and detrain their moisture there. It suggests that the better performance of the IFS in comparison to the CMIP5 models described next is mainly due to its physics package. It also highlights that the model's behavior is consistent across horizontal resolutions.

The CMIP5 models reveal a variety of CF profiles. Some models have a mean CF profile that resembles a stratocumulus-topped boundary layer more than a trade-wind cumulus layer (MPI-M, CCCma) or hardly produce any cloud at all (IPSL). Other models do a reasonable job at reproducing the mean profile (CNRM, MOHC, MRI, and less so BCC and NCAR-C4). Some models even show a hint of a second peak in cloud near 800 hPa (MRI, NCAR-C4). One may question whether the large underestimation of cloud depth in some models is related to using the BOMEX location rather than the Barbados location. Several models do have a somewhat drier free troposphere than what is observed. For the MPI-M model both locations are available, yet this difference in location does not correspond to a different cloud layer. Also in other models the bias in cloud depth is very likely unrelated to the difference in location, but reflects a larger issue in the parameterized physics.

That parameterized physics play a large role in cloud biases, rather than just a difference in large-scale environment, is exemplified by the fact that at first-order the mean CF profiles are not well separated by their corresponding RH profiles. For instance, one may look at the level at which relative humidity falls below 50%, which differs by more than a 100 hPa among the models (Figure 4c). In the BCC model, this level is much lower than in the MPI-M model, yet the BCC model has a much deeper cloud layer. Another example is that both the MPI-M and the CCCma models have a very shallow cloud layer, yet they differ markedly in the structure of the RH profile below 700 hPa. Furthermore, several models have a sharp decrease in RH just above cloud base (MPI-M, BCC, IPSL, MOHC, MRI), but not all of them all predict a single cloud layer resembling stratocumulus.

One of the challenges with finding a relationship between the CF profile and its mean environment is that the mean CF profile is for some models a poor reflection of the instantaneous CF profile. The CF distribution at a given level is often skewed, whereby many models have a median profile that is zero throughout the entire layer (note the dotted profiles in Figure 4a). This means that models alternate between a few cases where certain height levels support large CF's, but many more cases where cloud is absent at both levels. In the observations, CF is only zero at both 925 and 825 hPa 3% of the time (Table 2), whereas in the models CF is zero at both levels 1–65% of the time. These findings will be elaborated upon in section 4.

Although many models have a peak in CF near the LCL in their mean profiles, their relative distribution of cloud across the cloud layer can be very different in single-timestep profiles. Changes in the distribution of

cloud may be analyzed by looking at the ratio of CF to CF_p in single-timestep profiles, whereby CF_p is CF at the level of approximate cloud base ($p_{CFmax,}$ in Table 2). Figure 4b shows the mean, median, and interquartile range of distributions of this ratio. This for instance reveals that MPI-M occasionally produces cloud one level above p_{CFmax}. CF at those higher levels can be up to 10 times larger than CF at p_{CFmax}. The same is true for the BCC, IPSL, CNRM, and MRI. Other models tend to produce a CF profile that is always similarly shaped. For instance, the MOHC has a profile whereby CF at every level is close to CF at $p_{CFmax,}$ because the ratio of CF to CF_p is always close to 1.

As discussed in section 1, Brient et al. (submitted manuscript, 2015) introduced a parameter γ to evaluate the shape of the CF profile in regions with moderately subsiding motion, where γ is defined as $CF_{950}/(CF_{950} + CF_{850})$. A small γ reflects a top-heavy CF profile whereas a large γ reflects a bottom-heavy CF profile. A modified version of this parameter, which we denote as γ*, uses pressure levels of 925 and 825 hPa instead, which better targets the levels at which CF maximizes in the observations. These levels also better target CF in the models, because CF at 950 hPa is often zero. γ* derived from single-timestep output gives Figure 5a. Some models show a similar γ* distributions as the observations, notably, the ECMWF, ECMWF-LI, BCC, and the NCAR models. However, other models reveal a distribution that is much more bimodal. They either predict a bottom-heavy profile without cloudiness further aloft ($\gamma^* = 1$), which the observations indicate is true 20% of the time, or they predict a profile with cloud at 825 hPa but not at 925 hPa ($\gamma^* = 0$), which the observations indicate is true only 7% of the time. This means that models fail to produce cloudiness near the LCL and cloudiness aloft simultaneously, which shows that they insufficiently couple these two components (except for MOHC, which overestimates the coupling).

When the profiles are first averaged to monthly means before γ* is derived, the distributions shift toward a more unimodal distribution for some models (Figure 5b). The mean γ* of these distributions is indicated with square markers at the top of the plot. A few models continue to be too bottom-heavy (MPI-M, CCCma, NCAR-C5), but for other models one could not have guessed that they are either top-heavy or bottom-heavy in the single-timestep output. For instance, MRI has a $\gamma* \geq 0.9$ more than 30% of the time in single-timestep profiles, but never in the monthly mean profiles. CNRM ends up with a distribution that is close to the observations when using monthly mean profiles, but has very few single-timestep profiles that have a γ* that is close to that observed. IPSL has an overall mean γ* of 0.43, which is roughly the observed value, but its monthly distribution of γ* largely deviates from that observed. This demonstrates that the shape of long-term mean CF profiles may not necessarily reflect the processes that control the vertical structure of cloud at single-timesteps.

4. Variability of Cloud

By looking at the shape of modeled cloud fraction profiles in single-timestep output rather than in long-term means, we find that several models do not produce cloudiness near cloud tops along with cloudiness near the LCL. These models produce cloud profiles that are either very bottom or very top-heavy, instead of distributing cloud evenly across the cloud layer. In the following, we look into more detail at the temporal variability in cloudiness at the two levels, p_{CFmax} and 825 hPa, and address seasonal variability in the cloud profile.

4.1. Temporal Behavior

The total variance in cloudiness near the LCL and near cloud tops (at 825 hPa) are listed in Table 2, along with their ratio. This confirms what Figure 4 also shows, namely, that all models except the ECMWF-LI, BCC, MRI, and NCAR-C4, have more variance in cloudiness near the LCL than in cloudiness aloft. Not only do models vary the wrong component of cloud, they also have too much variance on longer time scales. Figure 6 shows the percentage of variance in CF that is explained at a given time scale, plotted as a cumulative distribution that starts from 6 h up to 60 days. Six hours is chosen as the minimum, because it is the Nyquist frequency of the ECMWF short-range forecasts, which are available every 3 h. For the observations and all other models, frequencies higher than 6 h are disregarded. Figure 6 (left plot) shows CF_p for the models and CC_{LCL} for the observations, whereas the Figure 6 (right plot) shows CF_{825} for the models and CC_{ALOFT} for the observations. As an example, where the plotted distribution intersects the vertical dotted line, which corresponds to a time scale of 1 day, the percentage represents the contribution of all time scales less than one day to the total variance.

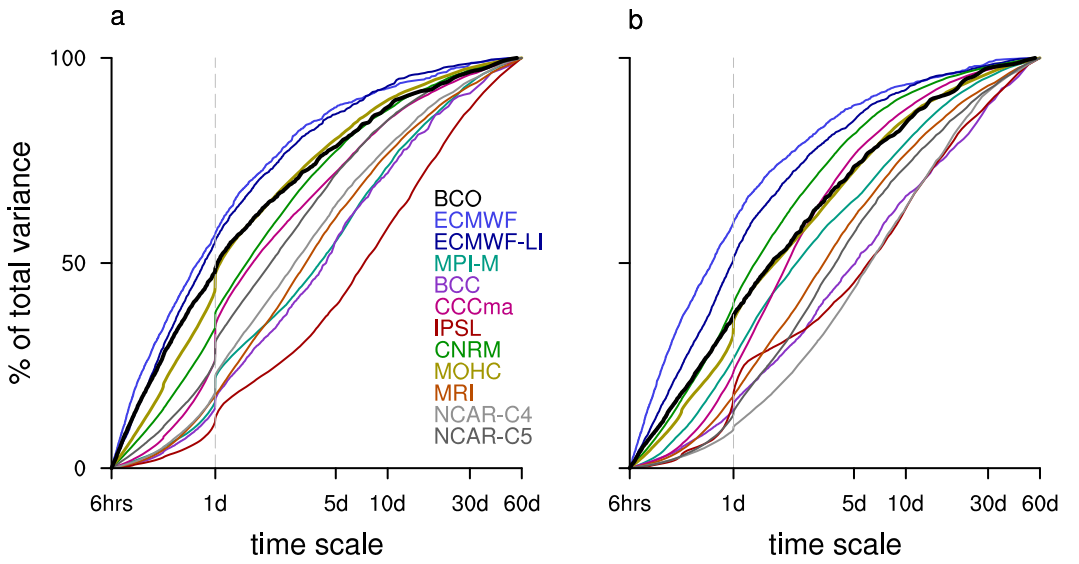

Figure 6. The percentage of variance explained as a function of time scale from 1 h to 60 days for cloudiness near cloud base (a) and cloudiness further aloft (b). For the BCO data, cloudiness is defined as CC_{LCL} (a) and CC_{ALOFT}, whereas for the models cloudiness is taken to be the cloud fraction at the level of CF_{p}, which is typically near cloud base at 925 hPa (a) and at 825 hPa (b).

Cloudiness near the LCL in the observations contains 50% of its variance on time scales less than 1 day and about 75% of its variance on time scales less than 5 days. As mentioned earlier, cloudiness near the LCL may vary relatively little on time scales of a few days and longer because of the fast adjustment of the mixed-layer to perturbations [*Stevens*, 2006; *Bellon and Stevens*, 2013]. This constrains the surface buoyancy flux and thereby the updraft core fraction. For instance, in Large-Eddy Simulations with different surface wind speeds and different surface moisture and heat fluxes the surface buoyancy flux is approximately the same [*Nuijens and Stevens*, 2012]. The idea behind these findings is that cumulus convection effectively regulates the frequency of parcels reaching saturation by keeping the mixed-layer top and the LCL close to one another. This negative feedback mechanism has also been called the cumulus-valve mechanisms [*Neggers et al.*, 2006].

Cloudiness in the ECMWF short and long integrations have more variance on short-time scales than the observations, whereas cloudiness in many CMIP5 models vary on longer time scales. Some models even contain 20–40% of their variance on time scales beyond 10 days. This suggests that models are too sensitive to processes that act on scales much larger than the scales associated with turbulence and convection.

Cloudiness aloft contains less variance on short-time scales than cloudiness near the LCL: about 35% compared to 50% is contained on time scales less than a day. This difference is captured by the ECMWF long integration, but not the short integration. Data assimilation procedures in the short integration may be responsible for removing structure in the layer that is established by large-scale processes. The MOHC and the two NCAR models also capture this difference in time scales between cloudiness near the LCL and further aloft. Other models, however, show that cloudiness varies similarly at the two levels. Also note that almost all the models show a hint of a diurnal cycle in cloudiness near the LCL (Figure 6a), which is not supported by the observations. Several models maintain that diurnality in cloudiness aloft (Figure 6b).

To further illustrate biases in modeled variability, a sample 30 day time series of cloudiness near the LCL is shown in Figure 7, with the single-timestep output in black and a 10 day running average in color. The BCO observations and ECMWF short-range forecasts are plotted in Figure 7 (top four plots), showing CC_{LCL} as well as the actual cloud fraction near cloud base: $CF_{p.}$ For the CMIP5 models, we do not have CC_{LCL} available, and instead use $CF_{p.}$

At the BCO, CC_{LCL} is observed to vary between 0 and 0.5 from 1 h to the next. However, the 10 day running mean is relatively invariant at a mean of about 0.3. The same relative invariance is true for $CF_{p.}$ For ECMWF and ECMWF-LI CF_{p} and CC_{LCL} are similar to the observations, by showing daily variations of a similar amplitude and a relatively constant running mean. One can note that at a few time steps CC_{LCL} of the ECMWF

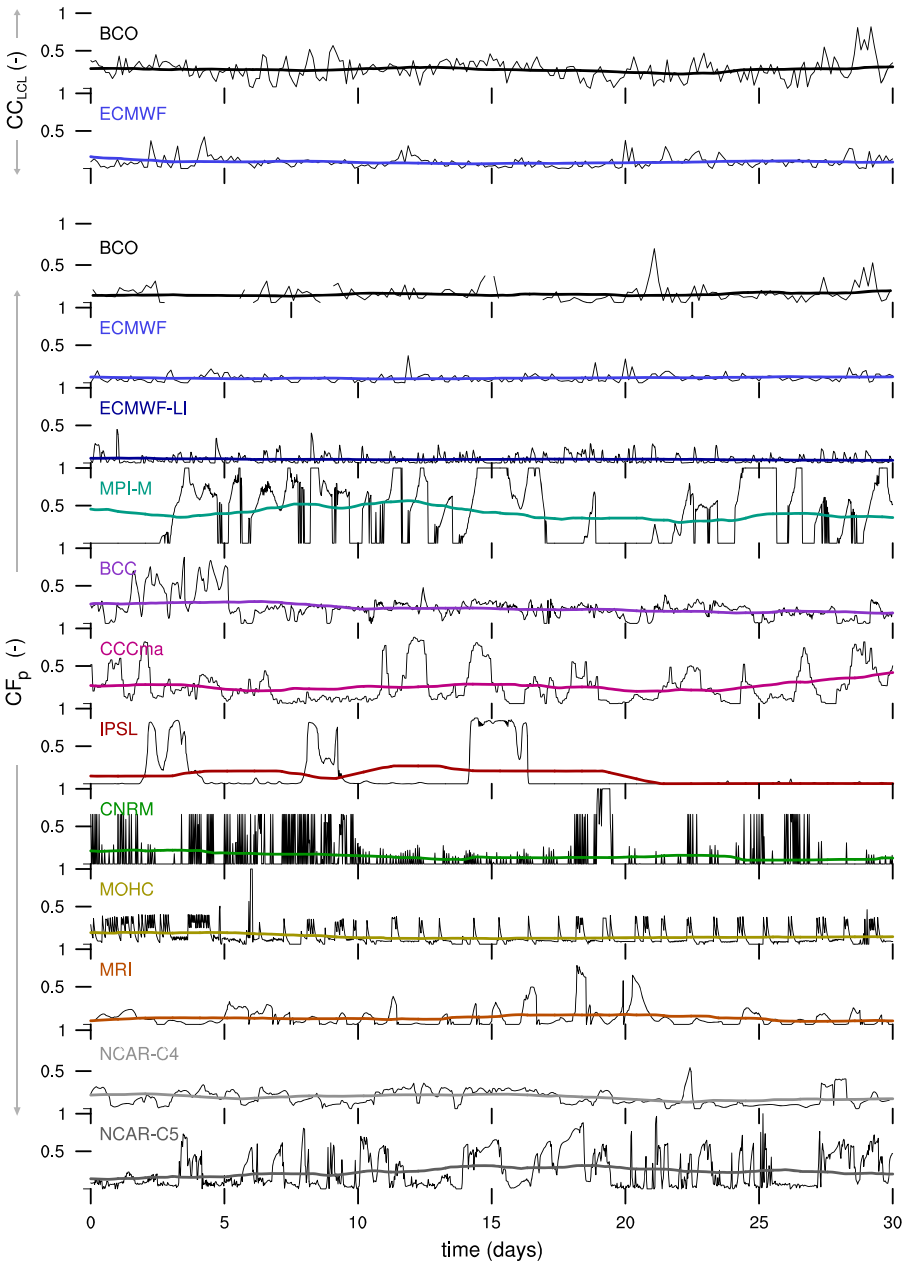

Figure 7. A 30 day time series of cloudiness from BCO data, the ECMWF model, and climate models is shown, where the 30 day period is randomly selected. For the BCO and ECMWF, both CC_{LCL} and CF_p are shown, whereas for the other models only CF_p is shown. The thick colored lines represent a 10 day running average.

shows larger variations than CF_p. This is not due to variations in cloud overlap, but because CF at two levels below 1 km exhibits larger variations (not shown).

Some CMIP5 models reproduce the invariance of CF_p in its running mean, for instance MOHC, CNRM, MRI, and NCAR-C4. However, biases at shorter time scales remain: there is a questionable diurnal cycle in MOHC; the CNRM and MRI have extended periods of zero cloudiness; and CNRM has a questionable upper limit in CF of about 0.7. In other models, the MPI-M, CCCma, and IPSL models, CF can reach large or small values that last for days and longer, which leads to a trend in their running mean.

One may question whether models that are developed to make climate predictions should also be able to predict such short timescale variability correctly. However, parameterized processes should act at the time

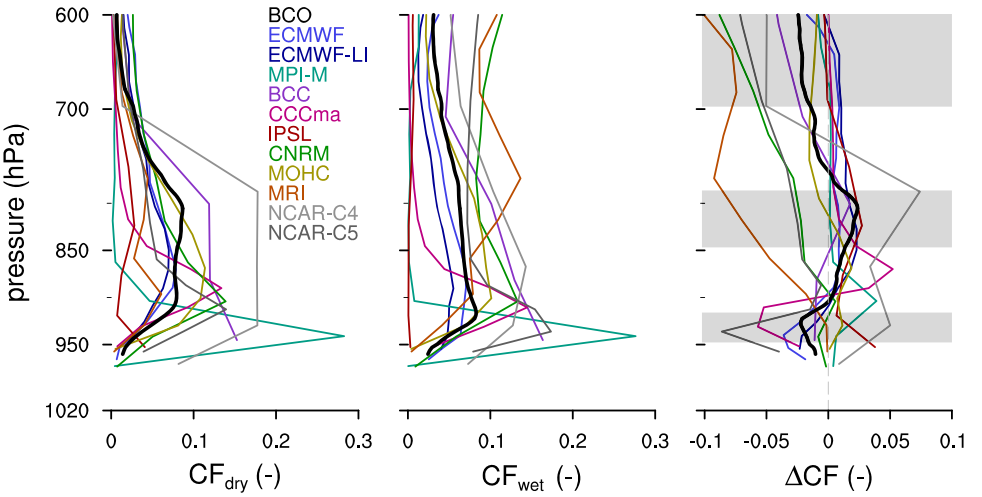

Figure 8. The mean CF profile of the months January–March (dry season), of the months September–November (wet season) and $\Delta CF = CF_{dry} - CF_{wet}$ is shown, from left to right. Between these months, the contrast in low-level cloudiness and meteorological parameters such as large-scale subsidence, lower tropospheric stability, and winds is the largest [*Brueck et al*., 2015]. The gray-shaded areas indicate the three regions in which CF is observed to change across season: near cloud base, near the trade-wind inversion, and in the free troposphere.

scales that they matter. These figures illustrate that in the observations such time scales may be short (cloudiness near the LCL) and that models do not capture such processes adequately. This resonates with studies using the Cloud-Associated Parameterizations Testbed (CAPT) and Transpose AMIP, which show that climate errors begin to manifest in very short forecasts [*Ma et al*., 2013]. Such short timescale variability may also impact radiative heating rates. Radiative heating rates are calculated less frequently than other physical processes, for instance every few hours. The large variability in cloudiness in Figure 7 may lead to biases in long-term radiative fluxes, which physically do not match the corresponding mean cloud profile.

4.2. Seasonality

An example of long-term biases is the comparison of observed and modeled contrasts between the dry and the wet season. *Nuijens et al*. [2014] found that both seasons have a comparable $CC_{LCL,}$ whereas CC_{ALOFT} is larger during the dry season, which experiences on average large-scale subsiding motion. The mean CF profile of the months January–March (dry season) versus September–November (wet season) are plotted in Figure 8. Also plotted is the profile of their difference, the dry season minus the wet season ($\Delta CF = CF_{dry} - CF_{wet)}$.

The mean LCL during the wet season is lower, because relative humidities are higher. Therefore, the peak CF during the wet season is lower, which can be seen from the negative ΔCF at heights below 920 hPa. It may also reflect rain which has not been captured by the filtering procedure, and which is more pronounced in the wet season. ΔCF is positive between 800 and 850 hPa near the inversion, which shows that deeper clouds with tops near the inversion and stratiform outflow are more common during the dry season. At heights above 800 hPa, ΔCF is negative again, indicative of deep convection, which is more common in the wet season. Despite this deep convection, the wet season has less cloud between 800 and 850 hPa, which means that less cumuli reach heights of 2–4 km. This may be caused by nearby deep convection, which induces compensating downdrafts, which in turn suppress the vertical development of surrounding cumuli. The wet season therefore has on average more passive cumuli confined to heights near the LCL.

Seasonality is thus pronounced at three different height ranges: $\Delta CF < 0$ below 920 hPa (near the LCL); $\Delta CF > 0$ between 920 and 800 hPa (in the cloud and inversion layer); and $\Delta CF < 0$ above 800 hPa (in the free troposphere). This trimodal structure is only captured by the BCC model. A few other models capture changes at two height ranges. The ECMWF and ECMWF-LI correctly predict ΔCF near the LCL and in the cloud layer, but miss the signature of deep convection in the free troposphere. MOHC instead predicts ΔCF in the cloud layer and free troposphere, but misses the ΔCF signature near the LCL.

Most models capture at least the signature of ΔCF in the free troposphere, as well as a general deepening and flattening of the CF profile in the wet season. However, the seasonality in cloudiness near the LCL and in the cloud layer can be opposite to what is observed. For instance, for those models with the largest variance in cloudiness near the LCL (Figure 7), a seasonality in cloudiness at that level is also pronounced. MPI-M and IPSL have more cloudiness near the LCL during the dry season, whereas NCAR-C5 has more cloudiness near the LCL in the wet season. Furthermore, in the CNRM, MRI, and NCAR-C5 models, ΔCF is negative throughout much of the cloud layer. Although MRI and CNRM produce top-heavy profiles more frequently than other models—in doing so they are principally closer to observed behavior (Figure 5a)—they produce those top-heavy profiles in the wrong season. This suggests that rising vertical motion is important for convection in these models.

Hence, it appears that one set of models produces more cloud when the large-scale vertical motion is subsiding, with a humid layer near cloud base, but a drier cloud layer aloft (MPI-M and IPSL). Another set of models produces more cloud when the large-scale vertical motion is rising and the cloud layer is humid (CNRM, MRI). The tendency of the models to either produce more cloud by making stratocumulus or by making deeper convection likely reflects that parameterization efforts in the past have focused more on these regimes than on the intermediate trade-wind cumulus regime.

5. Summary and Conclusions

Ground-based observations collected at Barbados have provided new insight into two aspects of trade-wind cloudiness: (a) the structure of the cloud layer and (b) its variability across a range of time scales. These insights provide a framework to evaluate single-timestep output from models at a single grid point near Barbados.

The observations show that the vertical cloud fraction profile is marked by two important levels. The first is located near the LCL and the second is located near the tops of the deepest cumuli, underneath the trade-wind inversion. Near the LCL cloudiness contributes substantially (two-thirds) to the total projected cloud cover. Cloudiness near cloud tops contribute another third to cloud cover, especially when stratiform outflow is present near cloud tops or when clouds deepen but not efficiently overlap, because they are irregularly shaped or slanted. Cloudiness near the LCL is relatively invariant when averaged over a few hundreds of kilometers (equivalent to a few days). Cloudiness further aloft instead contains more variance on time scales from a day to a week. Because cloudiness at both levels is common, the cloud fraction profile tends to be relatively constant with height, but a tendency for more top-heavy profiles is found during the dry season from December to May. Even when cloudiness near cloud tops is large, however, it is rare to find no corresponding cloudiness near the LCL.

Both short-range forecasts (1 day) and long-integrations (1 year) of the ECMWF IFS reasonably reproduce the observed cloud structure and its variability. This suggests that data assimilation procedures are not key to the performance of the IFS. The model tends to evenly distribute cloudiness across the cloud layer and the inversion, but thereby underestimates cloudiness near the LCL and below the trade-wind inversion. Larger cloudiness near the LCL may be achieved by considering that clouds at that level include not just detrained cumulus mass (passive cloud), but also the positively buoyant cores of clouds. Positively buoyant cores do not enter the cloud scheme in the ECMWF IFS, a feature that many models likely miss. Larger cloudiness below the trade-wind inversion may be improved by maintaining gradients at the inversion that help cap detrained moisture, as well as by considering cloud overlap assumptions.

The CMIP5 models reveal large differences in their mean cloud profiles. A handful of models reasonably reproduce the observations and the forecasts by distributing cloud over a layer that spans from the LCL to the mean trade-wind inversion. However, many models fail to produce the relative maxima of cloud at these levels. The other handful of models perform worse by producing a shallow cloud layer near the LCL only, which resembles stratocumulus. The larger values of cloudiness aloft in the dry season are captured by only a few models. Other models either do not have much cloudiness aloft at all or show larger values for cloudiness aloft in the wet season instead.

On shorter time scales, almost all models have larger biases in their cloud fraction profiles. Some models can only predict very bottom-heavy or very top-heavy profiles, which shows that models tend to alternate

cloud formation between different levels. All models (except the ECMWF, BCC, and NCAR-C5) predict zero cloudiness at both levels more than 10% of the time, whereas cloudiness in observations is only absent at both levels 3% of the time. For three models, this number is more than 50%. This leads to a large variance in cloudiness near the LCL, which in two-third of the models is larger than the variance in cloudiness aloft. The larger variance in cloudiness near the LCL is furthermore contained on time scales longer than a day, with some models even showing considerable variance on time scales beyond 10 days. This suggests that models do not capture turbulence and convective processes that appear to constrain cloudiness near the LCL in nature. Instead, they appear sensitive to processes that act on larger scales (longer time scales).

Because a model's monthly mean profile is not always representative for its single-timestep behavior, it may not reflect the model's parameterized physics. For instance, many models show that cloud is evenly distributed across the cloud layer in long-term means, whereas single-timestep output shows that models vary between very bottom-heavy or top-heavy profiles. Hence, the mean cloud profile may not reveal how a model tends to distribute moisture and cloud vertically. The single-timestep behavior also suggests that calculated radiative fluxes may be physically inconsistent with long-term mean cloudiness. Radiative heating rates are calculated less frequently than a single-timestep and may for instance occur during a period in which cloud fraction is zero, whereas cloud fraction may have been much larger before and after that period. Large biases may especially arise because the models do not randomly switch between cloud fractions of 0 and 1 (cloud blinking behavior), but produce small or large values of cloudiness for extended periods of time.

The large variance in the cloud base component of cloudiness in models, including the presence of a diurnal cycle and erroneous seasonality, has implications for the interpretation of cloud feedbacks. One may argue that models designed for climate prediction should not be expected to adequately capture cloud behavior on time scales less than a day. However, the short-time scale behavior does not simply behave as noise. Moreover, observations suggest that cloudiness is constrained by processes acting on such short-time scales. Therefore, parameterizations should act on those time scales too. The fact that they do not is evidence that models do not capture the mechanisms that underlie changes in cloudiness more generally. Hence, it is fair to ask whether clouds in models change in any way like nature under future forcing scenarios.

Acknowledgments

The BCO infrastructure is maintained by Ilya Serikov, Lutz Hirsch, Friedhelm Jansen, Bjoern Bruegmann, Monika Pfeiffer, and Holger Linne: without them this work would not have been possible. Many thanks go to Bjorn Stevens, Anton Beljaars, Peter Bechtold, and Robert Pincus for helpful discussions. Rodrigo Colpo is thanked for his work on the CMIP5 output, Sebastien Massart for his help with retrieving IFS data, and Andrew Gettelman for retrieving the BOMEX cfSites output for CAM4 and CAM5. L.N. appreciates the hospitality of NCAR and ECMWF for their hospitality during parts of this work. B.M. acknowledges support by the Regional and Global Climate Modeling Program of the U.S. Department of Energy's Office of Science, Cooperative Agreement DE-FC02–97ER62402. NCAR is sponsored by the National Science Foundation. The BCO data, the ECMWF short and long integrations, and the cfSites output for MPI-M, CAM4, CAM5 are available upon contacting the first author. The cfSites output for the remaining models can be downloaded from: http://cmip-pcmdi.llnl.gov/cmip5/data_portal.html.

References

Ahlgrimm, M., and M. Köhler (2010), Evaluation of trade cumulus in the ECMWF model with observations from CALIPSO, *Mon. Weather Rev.*, *138*(8), 3071–3083, doi:10.1175/2010MWR3320.1.

Bechtold, P., M. Köhler, T. Jung, F. Doblas-Reyes, M. Leutbecher, M. J. Rodwell, F. Vitart, and G. Balsamo (2008), Advances in simulating atmospheric variability with the ECMWF model: From synoptic to decadal time-scales, *Q. J. R. Meteorol. Soc.*, *134*(634), 1337–1351, doi: 10.1002/qj.289.

Bellon, G., and B. Stevens (2013), Timescales of the trade-wind boundary layer adjustment, *J. Atmos. Sci.*, *70*, 1071–1083.

Bony, S., and J.-L. Dufresne (2005), Marine boundary layer clouds at the heart of tropical cloud feedback uncertainties in climate models, *Geophys. Res. Lett.*, *32*, L20806, doi:10.1029/2005GL023851.

Bony, S., and K. A. Emanuel (2001), A parameterization of the cloudiness associated with cumulus convection; evaluation using TOGA COARE data, *J. Atmos. Sci.*, *58*, 3158–3183.

Brueck, H. M., L. Nuijens, and B. Stevens (2015), On the seasonal and synoptic time-scale variability of the North Atlantic trade wind region and its low-level clouds, *J. Atmos. Sci.*, *72*, 1428–1446.

de Rooy, W. C., P. Bechtold, K. Fröhlich, C. Hohenegger, H. Jonker, D. Mironov, A. Pier Siebesma, J. Teixeira, and J.-I. Yano (2013), Entrainment and detrainment in cumulus convection: an overview, *Q. J. R. Meteorol. Soc.*, *139*(670), 1–19, doi:10.1002/qj.1959.

Emanuel, K. (1993), A cumulus representation based on the episodic mixing model: the importance of mixing and microphysics in predicting humidity, in *The Representation of Cumulus Convection in Numerical Models, Meteorol. Monogr.*, edited by K. Emanuel, and D. J. Raymond, vol. 24, chap. 19, pp. 185–194, Am. Meteorol. Soc., Boston, Mass.

Gettelman, A., et al. (2010), Multi-model assessment of the upper troposphere and lower stratosphere: Tropics and global trends, *J. Geophys. Res.*, *115*, D00M09, doi:10.1029/2009JD013638.

Gregory, D., and P. R. Rowntree (1990), A mass flux convection scheme with representation of cloud ensemble characteristics and stability-dependent closure, *Mon. Weather Rev.*, *118*(7), 1483–1506, doi:10.1175/1520-0493(1990)118<1483:AMFCSW>2.0.CO;2.

Lock, A. P. (2009), Factors influencing cloud area at the capping inversion for shallow cumulus clouds, *Q. J. R. Meteorol. Soc.*, *952*, 941–952, doi:10.1002/qj.424.

Ma, H.-Y., et al. (2013), On the correspondence between mean forecast errors and climate errors in CMIP5 models, *J. Clim.*, *27*(4), 1781–1798, doi:10.1175/JCLI-D-13–00474.1.

Malkus, J. S. (1958), On the structure of the trade wind moist layer, *Pap. Phys. Oceanogr. Meteorol.*, *13*(2), 1–47.

McFarlane, N., J. F. Scinocca, M. Lazare, R. Harvey, D. Verseghy, and J. Li (2005), The CCCma third generation atmospheric general circulation model (AGCM3), CCCma internal report, Can. Cent. for Clim. Modell. and Anal., 25 pp., Univ. of Victoria.

Medeiros, B., and B. Stevens (2011), Revealing differences in GCM representations of low clouds, *Clim. Dyn.*, *36*, 385–399.

Nam, C., S. Bony, J.-L. Dufresne, and H. Chepfer (2012), The too few, too bright tropical low-cloud problem in cmip5 models, *Geophys. Res. Lett.*, *39*, L21801, doi:10.1029/2012GL053421.

Neggers, R., B. Stevens, and J. D. Neelin (2006), A simple equilibrium model for shallow-cumulus-topped mixed layers, *Theor. Comput. Fluid Dyn.*, *20*(5-6), 305–322, doi:10.1007/s00162-006-0030-1.

Nitta, T., and S. Esbensen (1974), Heat and moisture budget analyses using BOMEX data, *Mon. Weather Rev.*, *102*, 17–28.
Nuijens, L., and B. Stevens (2012), The influence of wind speed on shallow marine cumulus convection, *J. Atmos. Sci.*, *69*(1), 168–184, doi: 10.1175/JAS-D-11-02.1.
Nuijens, L., I. Serikov, L. Hirsch, K. Lonitz, and B. Stevens (2014), The distribution and variability of low-level cloud in the North Atlantic trades, *Q. J. R. Meteorol. Soc.*, *140*, 2364–2374, doi:10.1002/qj.2307.
Rasch, P. J., and J. E. Kristjansson (1998), A comparison of the CCM3 model climate using diagnosed and predicted condensate parameterizations, *J. Clim.*, *11*, 1587–1614.
Rauber, R. M., et al. (2007), In the driver's seat: Rico and education, *Bull. Am. Meteorol. Soc.*, *88*(12), 1929–1937, doi:10.1175/BAMS-88-12-1929.
Ricard, J. L., and J. F. Royer (1993), A statistical cloud scheme for use in an AGCM, *Ann. Geophys.*, *11*, 1095–1115.
Serikov, I., and S. Bobrovnikov (2010), Atmospheric temperature profiling with pure rotational Raman lidars, in *Recent Advances in Atmospheric Lidars*, edited by L. Fiorani and V. Mitev, Optoelectronic materials and devices, vol. 7, INOE, 149–216.
Sherwood, S. C., S. Bony, and J.-L. Dufresne (2014), Spread in model climate sensitivity traced to atmospheric convective mixing, *Nature*, *505*(7481), 37–42, doi:10.1038/nature12829.
Siebesma, A. P., et al. (2003), A large eddy simulation intercomparison study of shallow cumulus convection, *J. Atmos. Sci.*, *60*(10), 1201–1219, doi:10.1175/1520-0469(2003)60<1201:ALESIS>2.0.CO;2.
Slingo, J. M. (1987), The development and verification of a cloud prediction scheme for the ECMWF model, *Q. J. R. Meteorol. Soc.*, *113*, 899–927.
Stevens, B. (2006), Bulk boundary-layer concepts for simplified models of tropical dynamics, *Theor. Comput. Fluid Dyn.*, *20*(5-6), 279–304, doi:10.1007/s00162-006-0032-z.
Sundqvist, H., E. Berge, and J. E. Kristjansson (1989), Condensation and cloud parameterization studies with a mesoscale numerical weather prediction model, *Mon. Weather Rev. 117*, 1641–1657.
Tiedtke, M. (1989), A comprehensive mass flux scheme for cumulus parameterization in large-scale models, *Mon. Weather Rev.*, *117*, 1779–1800.
Tiedtke, M. (1993), Representation of clouds in large-scale models, *Mon. Weather Rev.*, *121*, 3040–3061.
VanZanten, M. C., et al. (2011), Controls on precipitation and cloudiness in simulations of trade-wind cumulus as observed during RICO, *J. Adv. Model. Earth Syst.*, *3*, M06001, doi:10.1029/2011MS000056.
Vial, J., J. L. Dufresne, and S. Bony (2013), On the interpretation of inter-model spread in CMIP5 climate sensitivity estimates, *Clim. Dyn.*, *41*, 3339–3362, doi:10.1007/s00382–013–1725–9.
von Salzen, K., N. McFarlane, and M. Lazare (2005), The role of shallow convection in the water and energy cycles of the atmosphere, *Clim. Dyn.*, *25*(7-8), 671–688, doi:10.1007/s00382-005-0051-2.
Wu, T., R. Yu, F. Zhang, Z. Wang, M. Dong, L. Wang, X. Jin, D. Chen, and L. Li (2010), The Beijing Climate Center atmospheric general circulation model: Description and its performance for the present-day climate, *Clim. Dyn.*, *34*(1), 123–147, doi:10.1007/s00382-008-0487-2.
Yukimoto, S., et al. (2012), A new global climate model of the meteorological research institute: Mri-cgcm3 model description and basic performance, *J. Meteorol. Soc. Jpn.*, *90A*, 23–64, doi:10.2151/jmsj.2012-A02.
Zhang, G. J., and N. A. McFarlane (1995), Sensitivity of climate simulations to the parameterization of cumulus convection in the Canadian climate centre general circulation model, *Atmos. Ocean*, *33*(3), 407–446, doi:10.1080/07055900.1995.9649539.